# 3D Electromagnetic Reconfiguration Enabled by Soft Continuum Robots

Lucia T. Gan, Laura H. Blumenschein, Zhe Huang, Allison M. Okamura, Elliot W. Hawkes, and Jonathan A. Fan

Abstract—The properties of radio frequency electromagnetic systems can be manipulated by changing the 3D geometry of the system. Most reconfiguration schemes specify different conductive pathways using electrical switches in mechanically static systems, or they actuate and reshape a continuous metallic structure. Here, we demonstrate a novel strategy that utilizes soft continuum robots to both dynamically assemble electrical pathways and mechanically reconfigure 3D electromagnetic devices. Our concept consists of using soft robotic actuation to conductively connect multiple subwavelength-scale metallic building blocks, which form into electromagnetic structures when joined together. Soft robots offer an exciting avenue for electromagnetic device construction because they can form complex, high curvature shapes from low-loss dielectric materials using straightforward manufacturing methods. As a proof of concept, we experimentally implement a helical antenna that can switch chirality through tendon actuation of a soft pneumatic continuum robot. Our work introduces a new paradigm for electromagnetic reconfiguration using soft robotic platforms.

Index Terms—Soft robot applications, soft robot materials and design, mechanism design, additive manufacturing.

## I. INTRODUCTION

ELECTROMAGNETIC (EM) devices are 3D systems with properties that depend on their geometry. Manipulating the physical structure of these systems can produce dramatic property changes and enable diverse functionalities. For example, structurally tuning an antenna's conducting elements can

Manuscript received September 10, 2019; accepted January 12, 2020. Date of publication January 28, 2020; date of current version February 7, 2020. This letter was recommended for publication by Associate Editor Hugo Rodrigue and Editor K.-J. Cho upon evaluation of the reviewers' comments. This work was supported in part by the National Science Foundation under Award 1637446, in part by the Air Force Office of Scientific Research under Award FA2386-17-1-4658, and in part by the National Science Foundation Graduate Fellowship Program, and a Stanford Graduate Fellowship. (Lucia T. Gan and Laura H. Blumenschein contributed equally to this work.) (Corresponding author: Lucia Gan.)

- L. T. Gan and J. A. Fan are with the Department of Electrical Engineering, Stanford University, Stanford, CA 94035 USA (e-mail: luciagan@stanford.edu; jonfan@stanford.edu).
- L. H. Blumenschein and A. M. Okamura are with the Department of Mechanical Engineering, Stanford University, Stanford, CA 94035 USA (e-mail: lblumens@stanford.edu; aokamura@stanford.edu).
- Z. Huang is with the Department of Electrical and Computer Engineering, University of Illinois at Urbana-Champaign, Urbana, IL 61801 USA (e-mail: zheh4@illinois.edu).
- E. W. Hawkes is with the Department of Mechanical Engineering, University of California, Santa Barbara, CA 93106 USA (e-mail: ewhawkes@engineering.ucsb.edu).

This letter has supplementary downloadable material available at http://ieeexplore.ieee.org, provided by the authors.

Digital Object Identifier 10.1109/LRA.2020.2969922

modulate its resonance frequency, radiation pattern, polarization, and bandwidth [1]. Dynamic reconfiguration is essential in radio frequency (RF) EM systems to maximize communication fidelity and energy transfer, particularly in highly variable or electromagnetically crowded environments.

To date, most reconfigurable RF systems focus on one of two separate approaches. The first is based on dynamically switching electrical connections within a static layout of wires or antenna elements using switching components like transistors [2], [3], PIN diodes [4], MEMS switches [5], microfluidic systems [6], [7], and phase change materials [8]. The second approach uses mechanical actuation schemes to physically manipulate a continuous 3D metallic structure. Shape memory materials [9], origami folding techniques [10]–[13], physical manipulation [14]–[17], and robotic growth mechanisms [18] have been proposed or employed to transform 3D EM devices into various geometries.

These reconfiguration mechanisms are typically restricted to 2D substrate-based form factors with switches that suffer from nonlinearities or temperature sensitivity, or to materials, such as liquid metals, with poor conductivity that exhibit suboptimal microwave performance. Mechanical changes in antenna structure can deliver the most dramatic variations in antenna characteristics, but in general, reversible mechanical reconfiguration is challenging to design, actuate, and physically implement in a practical, reliable, and cost-effective manner [1]. Mechanical actuation schemes that change conductor length, including our prior work on a tunable soft robotic monopole antenna, are only relevant for modulating the frequency of simple linear antennas [6], [7], [16]–[18]. Most designs are limited to simple linear translations or revolute joints that cannot achieve complex shape changes. Soft robotics can offer an alternative solution to many of these challenges.

Helical antennas are one example where soft robotics can provide the large shape change needed to produce meaningful reconfiguration. Helical antennas are commonly applied to wireless communication systems for GPS, satellites, and radar due to their directional radiation and resistance to the Faraday effect and atmospheric conditions. A helix's intrinsic chirality enables selective interactions with waves of right- or left-handed circular polarizations, and active handedness switching would allow devices to dynamically access both polarization-dependent interactions. The ability to modulate polarization sense can increase system capacity, improve signal diversity, and reduce interference [1], but it is challenging to achieve this kind of reconfigurability using electrical switching strategies without

2377-3766 © 2020 IEEE. Personal use is permitted, but republication/redistribution requires IEEE permission. See https://www.ieee.org/publications/rights/index.html for more information.

accompanying changes in impedance and frequency characteristics. Mechanical designs may be able to bypass these challenges. Previously, polarization switchable helices have been realized by mechanically twisting a continuous conductive line around a central axis to switch a right-handed helix to a left-handed one [12]–[14], and by changing the deformation direction of a planar spiral [15]. These designs have limited reliability because they reshape a continuous line of copper, which can achieve a continuum of states beyond the desired helix and can lead to metal fatigue and plastic deformation upon multiple switching cycles.

In this paper, we demonstrate a novel and complementary strategy that leverages robotic reconfiguration approaches to dynamically assemble and mechanically reconfigure 3D RF devices using soft continuum robots. A static layout of conductive antenna elements is joined into continuous electrical pathways through 3D shape transformations using soft robotic actuation techniques. First, we present the design of a shape changing soft robot that uses tendon actuation and multi-element conductors to enable antenna reconfiguration (Section II). Next, we present the design of a helical antenna that can dynamically switch chirality as a proof of concept (Section III). Lastly, we present the experimental implementation of the soft robotic helical antenna and comparisons to simulation (Section IV).

## II. SHAPE CHANGING SOFT ROBOT ANTENNA DESIGN

#### A. Soft Robot Backbone

Soft robots serve as an ideal scaffold for RF applications because they are composed of elastomeric polymers, inextensible plastics, or textiles [19], which are all electromagnetically transparent. Here, a soft inflated continuum robot forms the backbone of the antenna. The soft pneumatic backbone is constructed from a thin low-density polyethylene (LDPE) tube that, when inflated, can be shaped by the relative length change of a path on the body through buckling [20]. Pneumatically driven soft robot antennas can be deflated into a compact, lightweight package that is easily transported and deployed where needed. This property could be applied to search and rescue applications where weight and volume must be minimized. Lightweight, collapsible antennas that can be stowed and deployed could be especially attractive as a payload for mobile robots requiring larger antennas for communications. In prior works, we have shown that this thin-walled pneumatically-driven structure can create a growing robot by everting material from the tip, which allows us to deploy large structures from small initial package sizes [20]. Previously, we exploited this growth feature to modulate frequency through changing antenna length [18]. In contrast, the emphasis in this current work is using soft robotic actuation methods to enable 3D shape change for antenna reconfiguration.

By judiciously routing actuators on the robot's exterior surface, we can strategically morph the antenna's geometry to change antenna properties like polarization. Shape change has previously been achieved with programmable latches that hold or release stored wrinkled material [20], pneumatic artificial muscles attached along a path that shorten when pressurized [21], [22], and tendons routed through rigid "stoppers"

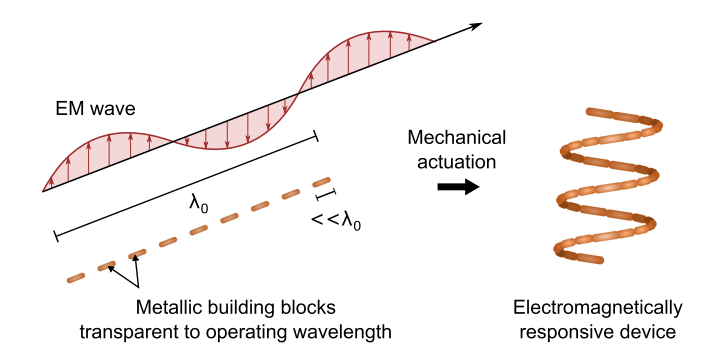


Fig. 1. Individual metallic subwavelength-scale building blocks (SuBBs) are electrically small and electromagnetically transparent to the target wavelength  $\lambda_0$  but form 3D devices responsive to  $\lambda_0$  upon mechanical actuation.

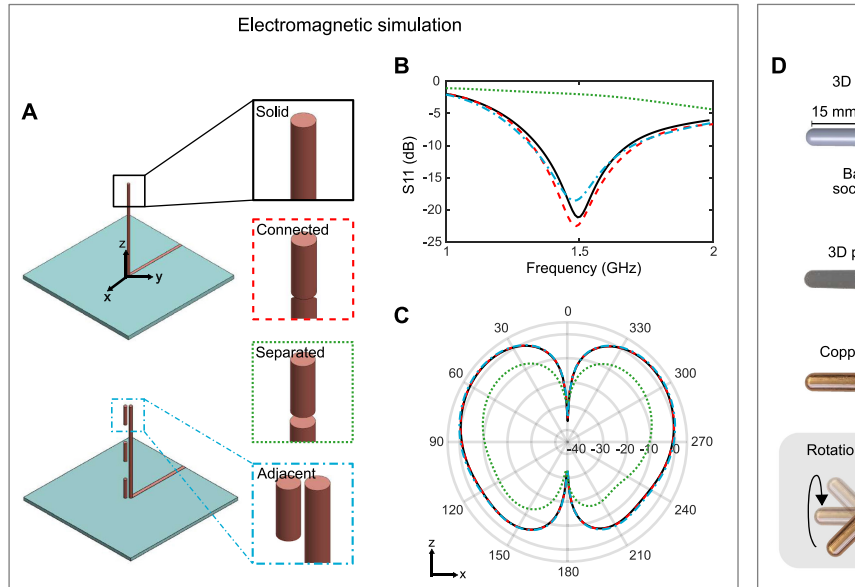
which limit the local deformation when the tendon is pulled [18], [23]. Tendon and stopper actuation is best suited for antenna reconfiguration because it allows us to create repeatable, precise, and reversible shape change, since the stoppers limit the local deformation once they contact and prescribe the change in path length during actuation. In addition, the stoppers act as essential components of the antenna switching, which is described in the following section.

#### B. Metallic Subwavelength-Scale Building Blocks (SuBBs)

In order to mechanically reshape the antenna's conductive element, we discretized a continuous metal conductor into multiple metallic subwavelength-scale building blocks (referred to as SuBBs from this point forward) that double as mechanical stoppers, which become electrically connected through physical contact (Fig. 1). The SuBBs are electrically small (i.e., small compared to a specified target free space wavelength  $\lambda_0$ ) and mechanically small (i.e., small compared to the length of the soft robotic structure). Due to its electrically small size, a SuBB by itself can be effectively electromagnetically transparent and will not couple to waves with wavelength  $\lambda_0$ . However, when groups of SuBBs are brought into contact, they join together into pre-programmed 3D metallic assemblies and form functional devices responsive to  $\lambda_0$  (Fig. 1). The mechanically small size of a SuBB serves to make the elements effectively mechanically "invisible" when disconnected, allowing us to construct rigid conductive EM structures without significantly affecting the overall deformability of the soft robot.

At the desired operating range for an ultra high frequency (UHF) radio antenna of 1 to 2 GHz, we designed copper SuBBs to have a length of 15 mm. At 1.5 GHz, this size is much smaller than the  $\lambda_0$  of 20 cm and corresponds to approximately  $\lambda_0/13$ , which exists in the Rayleigh scattering regime. For these SuBBs, the scattering cross section is very small and effectively EM transparent.

To investigate the effects of converting continuous metallic structures into equivalent assemblies of discrete SuBBs, we simulated a linear quarter-wave monopole operating at 1.5 GHz with different conductor configurations. Though our target design is a helical antenna, we analyzed a linear monopole due to its predictable and simple resonant behavior. Fig. 2A–C show that



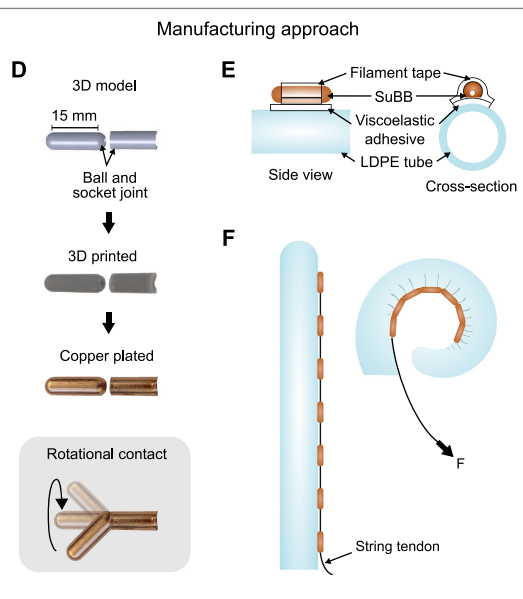


Fig. 2. (A) Analysis for the conversion of a monopole antenna from solid copper (solid black) to interconnected SuBBs (dashed red), to separated SuBBs (dotted green), then to interconnected SuBBs with disconnected adjacent elements (dotted blue). (B) Simulated return loss (S<sub>11</sub>) spectra and (C) radiation patterns for the conversion of a monopole antenna from solid copper to SuBBs. The polar plot is in units of dB. (D) Metallic SuBB fabrication involves generating a CAD model and 3D printing the structure in photopolymer resin. A thin layer of copper is plated on the resin scaffold. Ball and socket joints on alternating SuBBs ensure rotational contact from many incoming angles. (E) SuBBs are attached to a soft robot made of LDPE tubing using a viscoelastic adhesive. Fiber-reinforced filament tape is taped over the SuBB to ensure it is bonded. (F) Concept for a soft robotic antenna with a multi-element conductor and a soft inflatable robot backbone. The conductive pathway is fully connected during shape change when a pulling force is applied to a tendon that is threaded through the SuBBs.

the conversion from solid copper (solid black) to 15 mm long interconnected SuBBs (dashed red) results in a slight decrease in simulated return loss (Fig. 2B) and no change in far-field radiation characteristics (Fig. 2C). When the SuBBs comprising the antenna are separated by only 1 mm (dotted green), the resonance at 1.5 GHz is eliminated (Fig. 2B) and the radiated power drops by an order of magnitude (Fig. 2C), providing an off state for the system. Disconnected SuBBs placed adjacent to the active device (dotted blue) result in a slight increase and red-shift in return loss at resonance (Fig. 2B) and no change in the far-field radiation pattern (Fig. 2C), confirming that individual discrete SuBBs are effectively transparent to devices operating at  $\lambda_0$ , even when placed in the near-field of the device.

Both the electrical and mechanical invisibility of the SuBBs are important for the reconfiguration of the antenna. Creating a conductor out of discrete elements that can be separated and become electromagnetically transparent allows us to place multiple actuator paths of SuBBs, and therefore multiple potential antennas, on a single robot without significant interference between them. The mechanical transparency of the SuBBs allows the underlying soft robot to form different programmed shapes when different actuators are pulled, while maintaining its soft, deformable properties.

## C. SuBB and Tendon Actuator Manufacturing

The SuBB design ensures robust mechanical and electrical properties. Due to the skin effect at RF frequencies, EM waves

only propagate along the surface of a conductor and do not penetrate into the interior of the conductor if the metal is sufficiently thick. The skin depth of copper at 1.5 GHz is 1.7  $\mu$ m. Therefore, it is not necessary to form the SuBBs from solid metal, and we can leverage novel, lightweight, and low-cost rapid prototyping manufacturing approaches.

To manufacture the SuBBs, we print a photopolymer resin support (15 mm in length and 6 mm in diameter) through stere-olithography 3D printing (Formlabs Form 2) and encapsulate the 3D-printed scaffold with a coat of copper deposited by an electroless plating process (Fig. 2D). The plated copper is approximately 20 microns thick, which is many times thicker than the skin depth and offers the potential for high-performance RF operation due to copper's high conductivity. Adding alternating ball and socket-like joints to the connection points between SuBBs helps to ensure robust mechanical and electrical contact. These ball and socket joints allow for multi-directional contact and rotation, and are crucial to accommodate the high degrees of curvature necessary to produce continuous and smooth shapes that curl and twist because they can connect at many incoming angles.

The fabrication of microwave devices from a metal plated 3D-printed scaffold has been previously demonstrated for waveguides, air-core inductors, and other static 3D antennas [24], [25]. Additive manufacturing in conjunction with plating offers a lightweight, cost-effective, and fast-prototyping alternative to traditional antenna manufacturing methods. In the future, the versatility of 3D printing could produce a range of quickly fabricated SuBB shapes, from simple cylindrical segments like

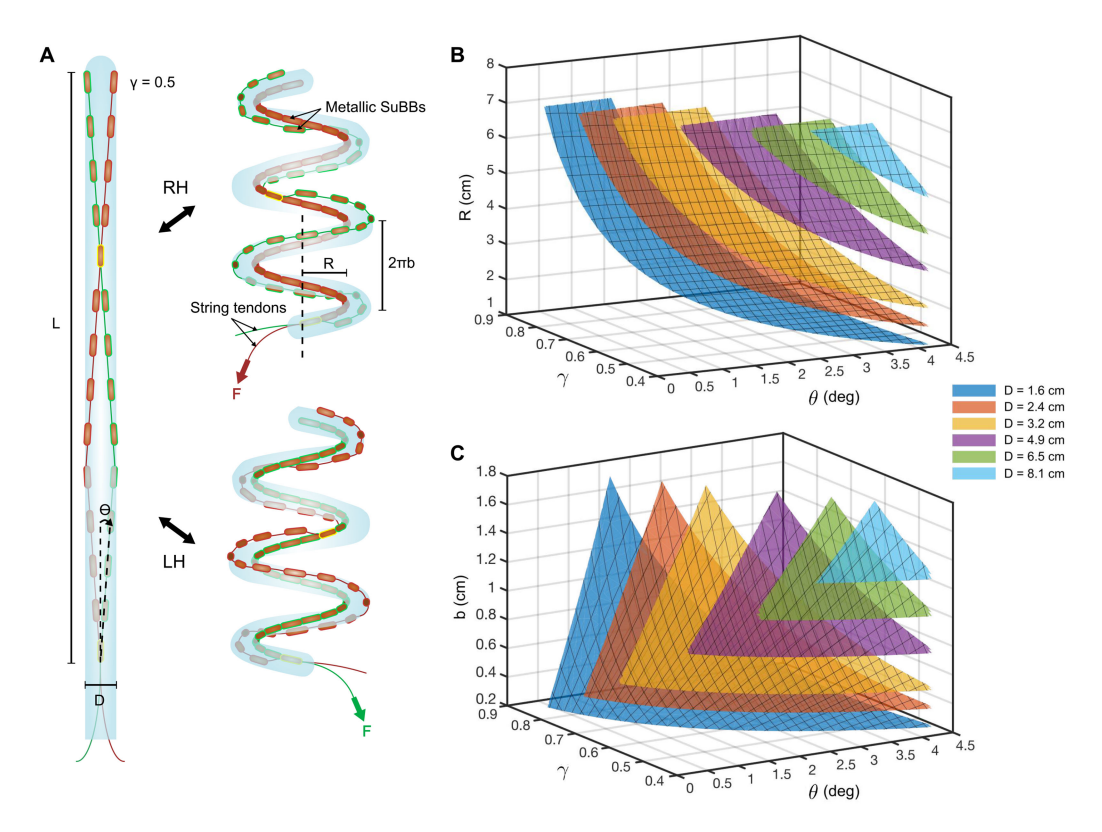


Fig. 3. (A) Detailed schematic of helical antenna described by parameters D,  $\theta$ ,  $\gamma$ , L, R, and b. Applying tension to a string tendon transforms the soft robot backbone from a straight configuration to a right-handed (RH) or a left-handed (LH) helix.  $\gamma$  is a dimensionless contraction ratio between the individual SuBB length and the distance between adjacent SuBBs. In this schematic, the spacing between SuBBs is two times the length of an individual SuBB, so  $\gamma=0.5$ . (B) Design space of feasible helix radii R and (C) normalized spacing distances b for permissible  $\theta$  and  $\gamma$  values for various fixed D values.

the ones demonstrated in this paper to alternative geometries tailored to specific applications.

Using the air-inflated LDPE tube as a backbone, SuBBs can be affixed along pre-programmed pathways on the body with a tendon threaded through them. The copper SuBBs are bonded to the thin-walled LDPE tubing using a soft viscoelastic adhesive (TrueTape LLC) and fiber-reinforced filament tape (Fig. 2E). Waxed braid is threaded through the copper SuBBs and serves as the string tendon actuator. Applying a pulling force on the string tendon shortens the distance between metallic SuBBs by buckling the plastic body until adjacent SuBBs unite and conductively connect. This buckling results in a bulk structural change, like a bend or a curve, while simultaneously assembling collections of SuBBs to form a device (Fig. 2F). Judicious placement of SuBB stoppers along the robot body results in complex and repeatable motions, such as curling or twisting, and the addition of more than one actuator routed on the same robot yields multifunctionality. The continuum robot body naturally allows for the creation of continuous and smooth shapes, which is particularly challenging for 3D reconfiguration [26].

# III. SOFT ROBOTIC HELIX ANTENNA DESIGN

## A. Helical Tendon Actuator Design

As a proof of concept, we used the design principles from Section II to implement a soft robotic helix antenna that switches chirality. Dynamic chirality switching of a helix is a particularly challenging system to mechanically reconfigure because it requires changing into the mirror image helix and typically entails significant manufacturing complexity.

Previous work in soft robotics has shown that routing the actuator in a uniform helical path around the soft body leads to both curvature and torsion of the robot backbone when actuated, resulting in a helix in 3D space. We previously proposed this actuation method for reshaping soft robots into helices with varying radii and pitch in [18] and [23], but did not develop a method for autonomous actuation, handedness switching or forming a metallized, conducting path when actuation occurs.

Including both right- and left-handed helical actuators on the exterior of the same soft robot body can enable chirality switching. This handedness selectivity is visualized in Fig. 3A. In its straight state, the antenna is inactive because the disconnected SuBBs are electromagnetically invisible. From the straight state, pulling an actuator that curls around the robot body in a right-handed direction results in a right-handed helical antenna, and vice versa. The SuBBs that form the opposite-handed helix are disconnected and do not interfere with the active helical device at its operation frequency. Since the tendons curl around the body in opposing directions, they physically cross over at multiple points on the robot body. The SuBBs where tendons overlap on the robot body are common to both configurations and are outlined in yellow in Fig. 3A. These shared SuBBs have multiple tendons

threaded through them and can present a potential future design tool, where the total number of conductor elements needed for multiple antenna configurations can be reduced by the placement of common, shared SuBBs where multiple actuator paths cross over. The different connection angles to a common SuBB is made possible by the ball and socket connection points and shown in the supplementary video.

## B. Actuation Requirements

As described above, a desired helix is achieved by applying tension to the corresponding tendon. As tension is applied, the tube buckles at discrete locations and continues bending at the buckled points until the SuBBS are brought into contact with one another. The moment needed to buckle is equal and opposite to the moment due to the internal pressure:

$$M = \frac{PD^3}{8} \tag{1}$$

where M is the moment, P is the internal pressure and D is the tube diameter. Since the tendons apply a force at the surface of the tube, the corresponding buckling force,  $F_B$ , is:

$$F_B = \frac{M}{D} = \frac{PD^2}{8}. (2)$$

Generally, the robot begins to buckle near the base of the robot when tendon tension is applied, so the SuBBs most proximal to the base connect first. The connected SuBBs limit further deformation as each more distal point actuates until the antenna is fully connected from base to tip. This sequential actuation is observed in the supplementary video, and causes the actuation force to increase as the shape is being formed, due to the need to pull the tendon through the curved path of the connected SuBBs. This increase in friction can be approximated with the capstan equation:

$$F_T = F_B e^{\mu\psi} = \frac{PD^2}{8} e^{\mu\psi} \tag{3}$$

where  $F_T$  is the tension force,  $\mu$  is the friction coefficient between the tendon and SuBBs, and  $\psi$  is the total angle swept out by connected SuBBs. Experimental measurements of  $F_T$  indicate  $\mu$  has a value of 0.4 when using waxed braid.

In our supplementary video, we demonstrate autonomous chirality switching of a helical antenna with two turns actuated using two DC gearmotors, one for each tendon. The internal pressure is set sufficiently high at P = 17 kPa so that the robot returns to the straight state between right- and left-handed configurations. We use waxed braid as the tendon material, since it provides a low coefficient of friction, reducing the capstan friction (Eqn. 3). The gearmotor is able to produce a peak torque of 2.5 Nm, sufficient to provide the 40 N of tension necessary to completely actuate into the helix. To autonomously change the chirality, we implement two feedback mechanisms: magnetic encoders to sense the position of the tendon and conductivity sensing to detect when the fully connected state is achieved. In a real use case, real-time measurements of the antenna properties could replace this conductivity sensing, but here we use the voltage difference between the base and tip of the antenna as

an indication that the device has been formed. Using this implementation, we were able to cyclically reconfigure between right-and left-handed states over 10 times without losing conductivity.

We note that by using mechanical actuation, we can enable dramatic variations in antenna characteristics but our reconfiguration speeds are relatively slow. In the above demonstration, it takes around 10 seconds to fully actuate, though this speed can be somewhat increased with a more powerful motor. As such, our platform is suitable for programming different 3D shapes over long time scales, and it is less applicable to systems requiring very fast modulation of EM responses. However, it remains useful for specific applications with complex geometry change requirements.

## C. Antenna Design Parameters

A helical antenna driven in axial mode radiates a circularly polarized beam off the end of the antenna along its axis. The direction of circular polarization corresponds to the physical direction of twist of the helix. To maximize the radiation in the axial direction, the phase difference of the current between each turn must be an integer multiple of  $2\pi$  so that the power radiated by each turn superimposes maximally. This  $2\pi$  phase shift constrains the radius R and normalized turn spacing b, identified on Fig. 3A, required for optimal operation for a wavelength  $\lambda_0$ , summarized as:

$$\frac{2\pi R}{\lambda_0} = \sqrt{\frac{4\pi b}{\lambda_0} + 1}. (4)$$

R is typically chosen to be  $\lambda_0/2\pi$  such that the circumference is equivalently  $\lambda_0$ , and b must be small compared to  $\lambda_0$  to preserve the relationship in Eqn. 4.

#### D. Actuator Design Parameters

To actuate the soft robot backbone into the desired helical geometry, precise routing of the actuators and metallic SuBBs is required and determined by four parameters: the diameter of the plastic tubing forming the robot body, D, the angle of the actuator with respect to the vertical axis,  $\theta$ , the contraction ratio,  $\gamma$ , and the straight tubing length, L, identified on Fig. 3A. The value of  $\gamma$  represents the contraction ratio between the individual SuBB length and the distance between adjacent SuBBs. The actuator parameters D,  $\theta$ , and  $\gamma$  control the antenna parameters R and  $\theta$  (Fig. 3B–C) with the relationship:

$$R = \frac{D\gamma(\cos(2\theta) - \gamma)}{1 - 2\gamma\cos(2\theta) + \gamma^2}$$

$$b = \frac{D\gamma\sin(2\theta)}{1 - 2\gamma\cos(2\theta) + \gamma^2}.$$
(5)

The fourth parameter L, the length of the tubing, only impacts the number of turns produced. The relationship between the four actuator parameters including the length, L, and number of turns, n, is:

$$n = \frac{L}{2\pi D} \frac{\sqrt{1 - 2\gamma \cos(2\theta) + \gamma^2}}{\cos(\theta)}$$
 (6)

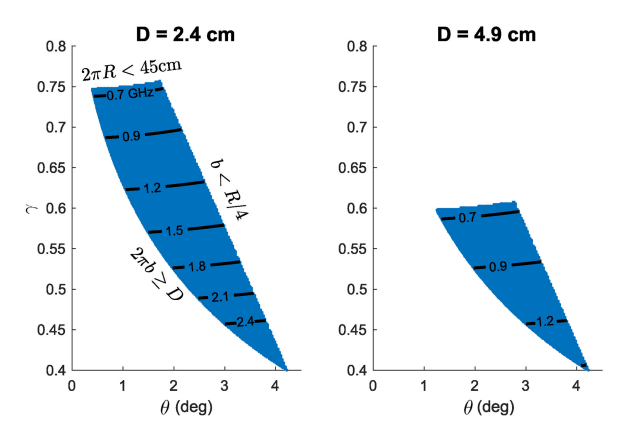


Fig. 4. Projections of the design space in Fig. 3B–C onto the  $\theta$ - $\gamma$  plane for two values of D. Level curves show the operating frequency based on the projected circumference of the helix. The boundary equations are shown on the left plot.

There are three actuator degrees of freedom  $(D,\theta,\gamma)$  to determine two antenna degrees of freedom (R,b), and varying each parameter produces a wide range of helices as detailed in [23]. While previous investigations have comprehensively studied helical actuation on soft inflatable robots for grasping strategies, we extended this line of analysis to focus only on designs that specifically support helical antenna performance.

1) Soft Robotic Antenna Design Space: With the aforementioned antenna geometry constraints in mind, we computed the permissible design space of helical antennas enabled by the soft robot for several values of D specified by various off-the-shelf LDPE tube diameters. We restricted  $R=\lambda_0/2\pi$  and  $b<\lambda_0/8\pi$ , or equivalently b< R/4, according to Eqn. 4. The maximum radius threshold corresponds approximately to a frequency threshold of 700 MHz. This frequency lower bound is motivated by the lower frequency limit of many radar applications. The normalized spacing, b, is lower bounded by  $D/2\pi$ , because the robot backbone cannot physically self-intersect.

The full design space for tube diameters between 1.6 cm and 8.1 cm is shown in Fig. 3B–C. We noticed that as D increases, the design space of feasible antennas decreases. Eqn. 5 indicates that D scales the size of the helix without changing the ratio between R and b. To remain within the design bounds as D increases, we require larger values of  $\theta$  and smaller values of  $\gamma$  to achieve the same antenna geometry. Fig. 4 shows the projection of the design space for two values of D onto the  $\theta - \gamma$  plane. We can see that, because of the scaling, the bounds for  $2\pi b \ge D$  and b < R/4 stay the same as the diameter changes. The bound for the minimum operating frequency,  $2\pi R < \lambda_o$ , becomes more restrictive as the diameter increase, a phenomenon shown by the frequency contour lines, as they require increasingly small values of  $\gamma$  to achieve the same  $\lambda_0$ . Therefore, devices that operate at higher frequencies cannot be accessed by using larger diameter tubes.

2) Sensitivity to Error: Finally, we investigated the sensitivity of the helix shape to small fluctuations in the design parameters. Some degree of manufacturing error arises when the SuBBs are manually affixed on the robot, so we conducted a sensitivity

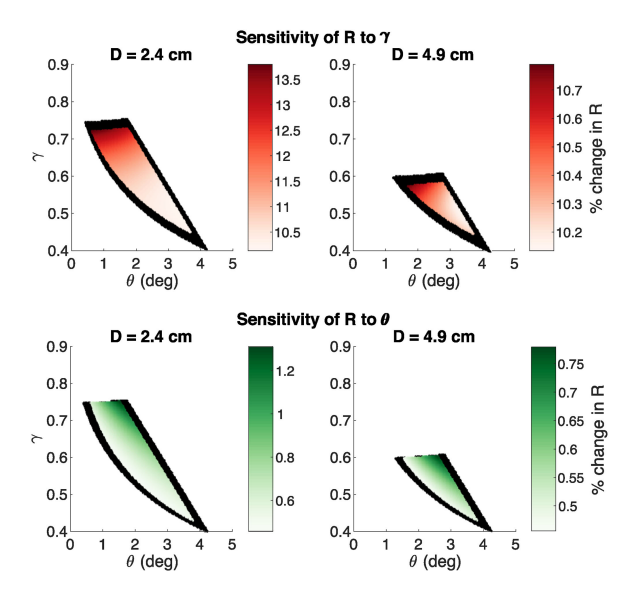


Fig. 5. Sensitivity of the helix radius, R, to variations in the actuator parameters  $\gamma$  and  $\theta$  for two values of D. Color intensity shows the percent change in the value of R caused by a change of 5% of the full range of  $\gamma$  (top) or  $\theta$  (bottom). Areas in black show where a 5% error causes a violation of one of the design space bounds.

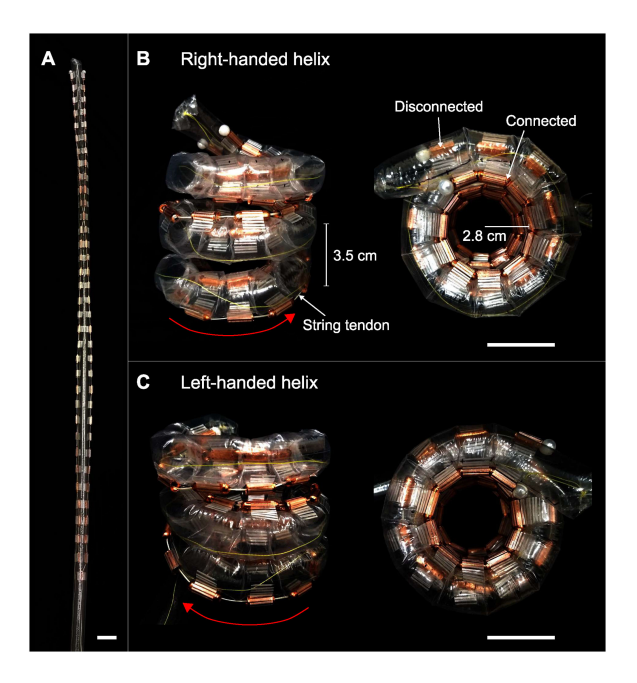


Fig. 6. (A) Straight configuration. (B) RH helical configuration. (C) LH helical configuration. Scale bars: 3 cm.

analysis that establishes the variability of the produced helix when the actuator parameters are changed slightly. We used a one-factor-at-a-time analysis, changing either  $\theta$  or  $\gamma$  by 5% of its full range for the smallest value of D ( $\pm 0.025$  for  $\gamma$  and  $\pm 0.24^{\circ}$  for  $\theta$ ). Since the radius, R, most directly influences the operating characteristics of the antenna, we focused on evaluating the percent change in the helix radius under this 5% parameter change (Fig. 5). We also show the areas of the design space that violate the design bounds if a 5% parameter error occurs,

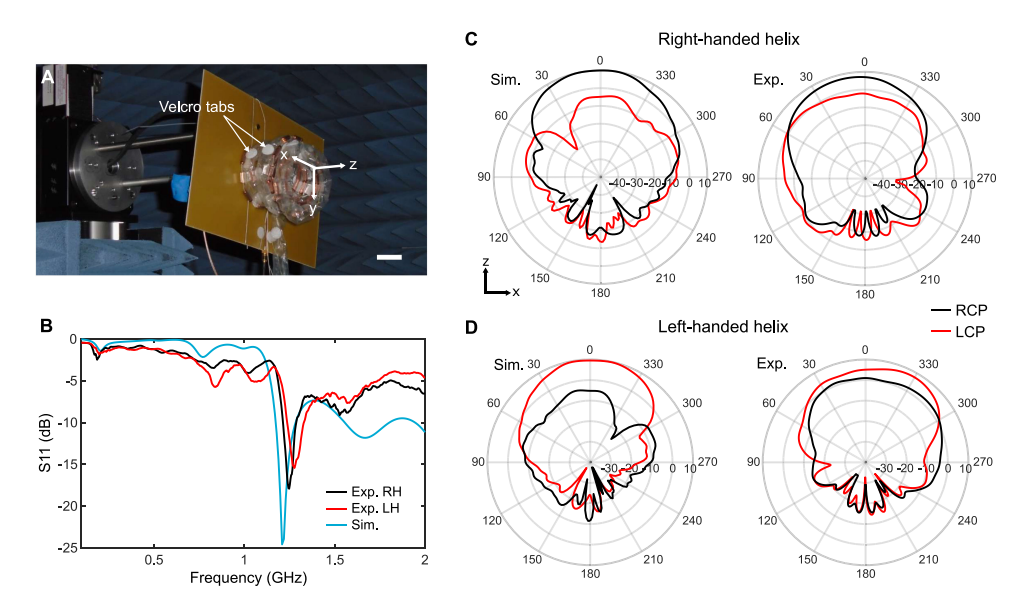


Fig. 7. (A) Image of antenna test setup in the anechoic chamber for radiation pattern measurements. Scale bar: 3 cm (B) Simulated and experimental return loss ( $S_{11}$ ) spectra for RH and LH helical configurations. (C) Simulated and experimental radiation patterns for RH helical antenna that displays transmission of right circularly polarized (RCP) waves and suppression of left circularly polarized (LCP) waves. (D) Simulated and experimental radiation patterns for LH helical antenna that displays transmission of LCP waves and suppression of RCP waves. In the direction of maximum gain, the experimental gain values for the opposite-handed circular polarization were transmitted with 6–10 dB less gain than the same-handed circular polarization. The patterns were measured at 1.5 GHz. The polar plots are in units of dB as a function of angle.

shown by the black margins in Fig. 5, defining more restrictive bounds based on the resulting shape errors.

Overall, the radius is an order of magnitude more sensitive to changes in  $\gamma$  than changes in  $\theta$ . Within the design space, the most sensitive regions occur at high values of  $\gamma$  and at relatively larger values of  $\theta$ . As D increases, the error increases proportionally. However, since the helix geometry scales proportionally with D, the percent error is unchanged. This analysis suggests regions of the design space with smaller values of  $\gamma$  and  $\theta$  will be more robust to manufacturing errors.

## E. Helical Antenna Manufacturing

From the soft robotic helical antenna design space, we selected an antenna design that permits operation at around 1.5 GHz. Only tubes with diameters less than and including 3.2 cm are able to form antennas with a circumference close to our desired wavelength, and the other parameter values were selected to mitigate sensitivity to manufacturing error. We constructed a robot backbone from a tube with D = 2.4 cm and affixed copper SuBBs in a helical path around the soft robot at an angle of  $\theta = 2.7^{\circ}$  from the vertical axis and  $\gamma = 0.5$ , which results in the 15 mm long SuBBs being spaced 15 mm apart from each other, visualized in the schematic in Fig. 3A. The length is L = 153 cm, which results in a helix with three turns. These parameters produce a helix with  $R \approx 2.8$  cm and  $b \approx$ 0.6 cm with 13 SuBBs per turn (Fig. 6A–C). Selecting a turn spacing that is close in value to the inflated robot diameter (i.e. near the  $2\pi b = D$  design bound) provides additional mechanical robustness, because each turn is physically supported by the one beneath it, ensuring uniformity and repeatability between multiple switching cycles. Velcro tabs between each turn ensure

further repeatability of the produced helices, enabling nearly bistable reconfigurability (Fig. 7A).

Our helix prototype is limited to three turns due to the high actuation force required to connect SuBBs. Increasing the number of turns would increase the antenna directivity, which could be beneficial depending on the application. This points to an inherent trade-off between pulling force and directivity using the tendon actuation method. Using lower friction tendons or alternative actuation strategies, like pneumatic artificial muscles [27], can potentially enable scaling to more turns.

## IV. EXPERIMENTAL RESULTS

Using the implemented helical antenna prototype from Section III, we compared its operating behavior to EM simulation at an operating frequency around 1.5 GHz.

Simulations of the return loss spectrum show that 75% or more of the input power is delivered to the antenna in a bandwidth spanning 1.2 GHz to 2 GHz (i.e.  $S_{11}$  below -6 dB). The simulated return loss is identical for both right- and left-handed antennas. The experimental data is collected through microwave scattering analysis using a vector network analyzer (Rohde & Schwarz ZNB20). We implemented a microstrip waveguide connected to a quarter wave transformer on the input end of the helix to match the antenna's input impedance to the 50  $\Omega$  coaxial cable impedance. The experimentally measured return loss spectra show very consistent patterns when switched from right- to left-handed and compares well to the simulation, demonstrating that our design concept achieves comparable impedance characteristics to its simulated counterpart (Fig. 7B). The difference in amplitudes between the simulated and experimental results can be attributed to surface roughness in the copper SuBBs,

contact resistance between SuBBs, and unaccounted attenuation and reflection from the surrounding environment.

Simulations show that the antenna transmits the same-handed circular polarization with a gain of approximately 10 dB and transmits the opposite-handed circular polarization with 15 dB less gain. The experimental far-field radiation pattern measurements were conducted in a near-field anechoic chamber at HRL Laboratories with a horn antenna as the transmitter (Fig. 7A). We evaluated the experimental far-field profile at 1.5 GHz. To characterize the polarization modulation of the antenna, we switched between its right-handed and left-handed helical configurations and measured the subsequent gain profiles for right and left circularly polarized (RCP and LCP) waves at azimuth angles from  $-180^{\circ}$  to  $180^{\circ}$  at  $\phi = 0^{\circ}$  (i.e. in the x-z plane of Fig. 7A). Gain considers both the efficiency and directivity of the antenna. The maximum RCP gain in the right-handed configuration is 8.1 dB (Fig. 7C) and the maximum LCP gain in the left-handed configuration is 7.3 dB (Fig. 7D), which is comparable to simulations. Experimentally, we observed that the opposite-handed polarization is transmitted with 6 to 10 dB less gain in the direction of maximum gain, or 10-25% of the power of the same-handed polarization. While the performance does not exactly match simulation, it demonstrates that the system has sufficient selectivity for the desired polarization. The discrepancy lies in the difficulty of fully simulating the effects of physically connecting many discrete SuBBs. These results indicate that our soft robotic antenna prototype has performance metrics in line with our simulated system.

## V. CONCLUSION

In summary, we presented a novel and general strategy for reconfiguring RFEM devices in 3D via the mechanical interconnection of SuBBs using a soft pneumatic continuum robot. We leveraged the electromagnetically and mechanically transparent behavior of SuBBs affixed to the exterior of a soft robot body, which remain unresponsive until assembled into a functional 3D device through string tendon actuation. These copper SuBBs are manufactured through low-cost additive manufacturing techniques combined with metal plating. We applied these principles to the dynamic chirality switching of a helix antenna, and experimental measurements validated that our reconfigurable antenna delivers comparable performance to its simulated counterpart.

#### ACKNOWLEDGMENT

We acknowledge T. Phan, T. Brockett, and A. Bekaryan for far-field antenna measurements at HRL Laboratories and J. Meisel for manufacturing assistance.

# REFERENCES

- [1] J. T. Bernhard, "Reconfigurable Antennas," *Synthesis Lectures Antennas*, vol. 2, no. 1, pp. 1–66, 2007.
- [2] L. N. Pringle et al., "A reconfigurable aperture antenna based on switched links between electrically small metallic patches," *IEEE Trans. Antennas Propag.*, vol. 52, no. 6, pp. 1434–1445, Jun. 2004.

- [3] T. Aboufoul, A. Alomainy, and C. Parini, "Reconfiguring UWB monopole antenna for cognitive radio applications using GaAs FET switches," *IEEE Antennas Wireless Propag. Lett.*, vol. 11, pp. 392–394, 2012.
- [4] S. Nikolaou *et al.*, "Pattern and frequency reconfigurable annular slot antenna using PIN diodes," *IEEE Trans. Antennas Propag.*, vol. 54, no. 2, pp. 439–448, Feb. 2006.
- [5] J. C. Maloney et al., "Switched fragmented aperture antennas," in Proc. IEEE Antennas Propag. Soc. Int. Symp., 2000, vol. 1, pp. 310–313.
- [6] J.-H. So, J. Thelen, A. Qusba, G. J. Hayes, G. Lazzi, and M. D. Dickey, "Reversibly deformable and mechanically tunable fluidic antennas," *Adv. Functional Mater.*, vol. 19, no. 22, pp. 3632–3637, 2009.
- [7] M. Kubo et al., "Stretchable microfluidic radiofrequency antennas," Adv. Mater., vol. 22, no. 25, pp. 2749–2752, 2010.
- [8] B. Gerislioglu, A. Ahmadivand, M. Karabiyik, R. Sinha, and N. Pala, "VO2-based reconfigurable antenna platform with addressable microheater matrix," Adv. Electron. Mater., vol. 3, no. 9, 2017, Art. no. 1700170.
- [9] S. J. Mazlouman, A. Mahanfar, C. Menon, and R. G. Vaughan, "Reconfigurable axial-mode helix antennas using shape memory alloys," *IEEE Trans. Antennas Propag.*, vol. 59, no. 4, pp. 1070–1077, 2011.
- [10] M. Nogi, N. Komoda, K. Otsuka, and K. Suganuma, "Foldable nanopaper antennas for origami electronics," *Nanoscale*, vol. 5, no. 10, pp. 4395– 4399, 2013.
- [11] G. J. Hayes, Y. Liu, J. Genzer, G. Lazzi, and M. D. Dickey, "Self-folding origami microstrip antennas," *IEEE Trans. Antennas Propag.*, vol. 62, no. 10, pp. 5416–5419, Oct. 2014.
- [12] X. Liu, S. Yao, B. S. Cook, M. M. Tentzeris, and S. V. Georgakopoulos, "An origami reconfigurable axial-mode bifilar helical antenna," *IEEE Trans. Antennas Propag.*, vol. 63, no. 12, pp. 5897–5903, Dec. 2015.
- [13] S. Yao, X. Liu, S. V. Georgakopoulos, and R. Schamp, "Polarization switchable origami helical antenna," in *Proc. IEEE Int. Symp. Antennas Propag.*, 2016, pp. 1667–1668.
- [14] S. Yao, X. Liu, and S. V. Georgakopoulos, "Segmented helical antenna with reconfigurable polarization," in *Proc. IEEE Int. Symp. Antennas Propag.* USNC-URSI Radio Sci. Meeting, 2017, pp. 2207–2208.
- [15] T. Kan et al., "Enantiomeric switching of chiral metamaterial for terahertz polarization modulation employing vertically deformable MEMS spirals," *Nature Commun.*, vol. 6, 2015, Art. no. 8422.
- [16] J. Costantine, Y. Tawk, and C. Christodoulou, "Reconfigurable deployable antennas for space communications," in *Proc. IEEE Int. Workshop Antenna Technol.*, 2014, pp. 151–154.
- [17] Y. Tawk, J. Costantine, F. Ayoub, C. Christodoulou, D. Doyle, and S. Lane, "Physically reconfigurable antennas: Concepts and automation," in *Proc. IEEE Int. Symp. Antennas Propag. USNC-URSI Radio Sci. Meeting*, 2017, pp. 419–420.
- [18] L. H. Blumenschein, L. T. Gan, J. A. Fan, A. M. Okamura, and E. W. Hawkes, "A Tip-Extending Soft Robot Enables Reconfigurable and Deployable Antennas," *IEEE Robot. Autom. Lett.*, vol. 3, no. 2, pp. 949–956, Apr. 2018.
- [19] D. Rus and M. T. Tolley, "Design, fabrication and control of soft robots," Nature, vol. 521, no. 7553, 2015, Art. no. 467.
- [20] E. W. Hawkes, L. H. Blumenschein, J. D. Greer, and A. M. Okamura, "A soft robot that navigates its environment through growth," *Sci. Robot.*, vol. 2, no. 8, 2017, Art. no. eaan3028.
- [21] J. D. Greer, T. K. Morimoto, A. M. Okamura, and E. W. Hawkes, "A soft, steerable continuum robot that grows via tip extension," *Soft Robot.*, vol. 6, no. 1, pp. 95–108, 2019.
- [22] M. M. Coad et al., "Vine robots: Design, teleoperation, and deployment for navigation and exploration," *IEEE Robot. Autom. Magazine*, 2019, doi: 10.1109/MRA.2019.2947538.
- [23] L. H. Blumenschein, N. S. Usevitch, B. H. Do, E. W. Hawkes, and A. M. Okamura, "Helical actuation on a soft inflated robot body," in *Proc. IEEE Int. Conf. Soft Robot.*, 2018, pp. 245–252.
- [24] J.-C. S. Chieh, B. Dick, S. Loui, and J. D. Rockway, "Development of a Ku-band corrugated conical horn using 3-D print technology," *IEEE Antennas Wireless Propag. Lett.*, vol. 13, pp. 201–204, 2014.
- [25] W. Liang, L. Raymond, and J. Rivas, "3-D-printed air-core inductors for high-frequency power converters," *IEEE Trans. Power Electron.*, vol. 31, no. 1, pp. 52–64, Jan. 2016.
- [26] D. C. Rucker and R. J. Webster III, "Statics and dynamics of continuum robots with general tendon routing and external loading," *IEEE Trans. Robot.*, vol. 27, no. 6, pp. 1033–1044, Dec. 2011.
- [27] J. D. Greer, T. K. Morimoto, A. M. Okamura, and E. W. Hawkes, "Series pneumatic artificial muscles (sPAMs) and application to a soft continuum robot," in *Proc. IEEE Int. Conf. Robot. Autom.*, 2017, pp. 5503–5510.